

Analysis of electro-permeation of hydrogen in metallic alloys

A. Raina, V. S. Deshpande and N. A. Fleck*

Cambridge University, Engineering Department, Trumpington St., Cambridge CB21PZ, UK

Keywords: Diffusion, Electro-permeation, Thermal desorption spectrometry, Trap binding energy

Summary

A reaction-diffusion type modelling framework is presented to analyse both electro-permeation (EP) and thermal desorption (TDS) measurements of hydrogen in metallic alloys. It is assumed that the kinetics of hydrogen motion is governed by diffusion through the lattice, along with trapping/detrapping at specific sites such as dislocations, grain boundaries etc. It is shown that the trapping and detrapping rates are typically much faster than the diffusion rate, and consequently a simplification of the governing equations suffices such that local equilibrium exists between lattice and trapped hydrogen. Using this local equilibrium assumption we then present an asymptotic analysis of the governing kinetic equation for the EP test. This asymptotic analysis reveals that four regimes of behaviour exist, ranging from negligible trapping to the complete filling of deep traps. The analysis suggests that EP tests should be so-arranged that three regimes of behaviour are spanned, in order to extract the relevant material properties associated with hydrogen transport. The numerical solutions presented in this study support the asymptotic analysis. The hydrogen kinetics framework is also deployed to analyse both EP and TDS tests on the same martensitic steel. The EP measurements all lie in regime I and are thus insufficient to uniquely determine both the trap density and binding energy. Reasonable agreement is obtained between measurements and numerical predictions of TDS tests using parameters estimated from the EP tests. Further improvements in measurements are required to confirm the fidelity of this modelling approach.

1. Introduction

The hydrogen kinetics in metallic alloys is typically measured via electro-permeation (EP) tests and thermal desorption spectrometry (TDS) tests. McNabb and Foster [1] presented a complete description of the kinetics that involves both diffusion of hydrogen through the lattice and the trapping and detrapping of the atomic hydrogen at trapping sites: these trapping sites include dislocations, grain boundaries and carbide particles. The

*Author for correspondence (Email: naf1@eng.cam.ac.uk).

EP and TDS tests are designed to estimate the densities of the trapping sites and the hydrogen binding energies for each type of trap.

There is a large literature on the analysis of hydrogen kinetics in metallic alloys. Most of these analyses are special cases of the McNabb and Foster [1] governing equations: readers are referred to Bhadeshia [2] and Song et al. [3] for overviews of the common modelling approaches. Broadly, three types of approaches are employed [4]:

(i) The so-called “standard theory” of Kissinger [5] is used to analyse TDS experiments. It is a special case of the McNabb and Foster formulation where both diffusion and trapping are infinitely fast and the rate governing process is detrapping of hydrogen from the trap sites.

(ii) Oriani [6] argued that the trap kinetics occurs on a much smaller time-scale than diffusion of hydrogen through the lattice. In this limit it is appropriate to assume that the lattice hydrogen is locally in equilibrium with the trapped hydrogen. Then, the McNabb and Foster [1] governing equations reduce to a Fickian diffusion equation with an effective or apparent diffusion coefficient that depends on the lattice and trapped hydrogen concentrations; see for example Sofronis and McMeeking [7] and Thomas et al. [8].

(iii) Turnbull and co-workers [9-11] have typically employed the “full” McNabb and Foster [1] equations where both diffusion through the lattice and trap kinetics are explicitly modelled. For example, Turnbull et al. [9, 10] successfully described the hydrogen permeation and thermal desorption response in steel by employing two classes of traps in the McNabb and Foster formulation. Turnbull [11] has extended this approach to take into account effects associated with the resistance that surfaces impose on hydrogen permeation.

In principle, both TDS and EP tests should give identical values of the relevant material parameters, viz. trap density and binding energy. However, few studies have attempted such comparisons. For example, Ha et al. [12] performed both TDS and EP tests on an X-70 grade ferritic/pearlitic steels (1% by volume pearlite): they employed the standard Kissinger theory to extract binding energy values from the TDS measurements and used a first order approximation of Fickian diffusion analysis (in the absence of trapping) for the EP tests. Thus, from this study it is difficult to ascertain whether the material parameters as extracted from the two types of tests are consistent.

In the present investigation we employ the McNabb and Foster [1] formulation to analyse both EP and TDS tests. The main aims are to (i) investigate the role of trap kinetics; (ii) present analytical solutions and associated maps illustrating the regimes of behaviour in EP tests and thereby elucidate the tests conditions that need to be achieved in order to extract the required material parameters uniquely from EP tests; and (iii) compare numerical predictions with existing measurements to illustrate inadequacies in both the existing data and analysis techniques.

2. Governing equations of hydrogen kinetics

Consider the transient diffusion of hydrogen atoms through a crystal lattice. In the absence of traps, Fickian diffusion gives the spatial and temporal evolution of the lattice concentration C_L . When diffusion occurs in the presence of traps, the modified one-dimensional diffusion equation reads as

$$\frac{\partial C_L}{\partial t} + \frac{\partial C_T}{\partial t} = D_L \frac{\partial^2 C_L}{\partial x^2}, \quad (1)$$

where $C_L(x,t)$ and $C_T(x,t)$ are the lattice and trapped hydrogen concentrations, respectively, as a function of a single spatial coordinate x and time t . Here $D_L = D_0 \exp(-Q/RT)$ is the lattice diffusion coefficient in terms of the temperature T , the lattice activation energy Q , the diffusion pre-exponential factor D_0 and the universal gas constant R . For the sake of simplicity, in the present study we shall analyse hydrogen kinetics in the presence of a *single* trapping species; readers are referred to Raina et al. [13] for the relevant equations with multiple trapping species.

Let θ_L be the fraction of lattice sites available to hydrogen that are occupied and θ_T be the corresponding fraction of sites within traps that are occupied by hydrogen. We can then write $C_L = \theta_L \beta N_L$ and $C_T = \theta_T \alpha N_T$, where N_L and N_T denote the number per unit volume of lattice atoms and trapping sites, respectively, while β and α are the number of available hydrogen sites per lattice atom and per trapping site, respectively. Equation (1) is then re-written as

$$\frac{\partial \theta_L}{\partial t} + \left(\frac{\alpha N_T}{\beta N_L} \right) \frac{\partial \theta_T}{\partial t} = D_L \frac{\partial^2 \theta_L}{\partial x^2}. \quad (2)$$

It now remains to specify an evolution law for the trapped hydrogen. Following McNabb and Foster [1], Raina et al. [13] express the kinetic law in the form

$$\frac{\partial \theta_T(x,t)}{\partial t} = [A\theta_L(1-\theta_T) - B\theta_T(1-\theta_L)]\nu, \quad (3)$$

where A and B are the probabilities of capturing and releasing a hydrogen atom per trap site, respectively, and ν is the atomic vibrational frequency. These probabilities can be evaluated using Boltzmann statistics when given the energy landscape of the hydrogen within the lattice and traps. We postulate an energy landscape as sketched in Fig. 1 where E_t and E_d are the trapping and detrapping enthalpies, respectively. Then the probabilities A and B follow as

$$A = \left(\frac{\beta N_L}{\alpha N_T + \beta N_L} \right) \exp \left\{ \frac{-E_t}{RT} \right\} \quad \text{and} \quad B = \left(\frac{\beta N_L}{\alpha N_T + \beta N_L} \right) \exp \left\{ \frac{-E_d}{RT} \right\}, \quad (4)$$

where $E_d = E_t - \Delta H$ and ΔH is the trap binding enthalpy; see Fig. 1. Equations (2) and (3) constitute a coupled set of partial differential equations in θ_L and θ_T for the kinetics of hydrogen motion within metallic alloys.

2.1 Local equilibrium between lattice and trapped hydrogen

Oriani [6] assumed that local equilibrium always exists between the hydrogen atoms at the lattice sites and the trap sites. For a finite value of $\partial \theta_T / \partial t$, in the limit of $\nu \rightarrow \infty$, Eq. (3) reduces to

$$\frac{\theta_T}{1 - \theta_T} = \frac{\theta_L}{1 - \theta_L} K, \quad (5)$$

where K is an equilibrium constant given in terms of the trap binding energy ΔH as

$$K = \exp \left\{ \frac{-\Delta H}{RT} \right\}. \quad (6)$$

In most practical cases, it is reasonable to assume that the lattice hydrogen concentration is small with $\theta_L \ll 1$ in which case Eq. (5) gives the trapped hydrogen occupancy fraction as

$$\theta_T = \frac{K \theta_L}{1 + K \theta_L}. \quad (7)$$

2.2 Non-dimensional kinetic equations

In order to illustrate the regimes of behaviour it is instructive to non-dimensionalise the above governing equations. In the present study we shall assume that the temperature of the specimen remains spatially uniform but varies with time such that $T = T_0 + \phi t$, where T_0 is the temperature at the start of the test at $t = 0$ and ϕ is a constant heating rate that is specified for the TDS tests but adopts the value $\phi = 0$ in the isothermal EP tests.

Consider a one-dimensional specimen of length L spanning a domain $0 \leq x \leq L$. Upon introducing the non-dimensional coordinate $\bar{x} \equiv x/L$ and a non-dimensional time $\bar{t} \equiv t D_0 / L^2$, Eq. (2) is written in non-dimensional form as

$$\frac{\partial \theta_L}{\partial \bar{t}} + \bar{N} \frac{\partial \theta_T}{\partial \bar{t}} = \bar{D}_L \frac{\partial^2 \theta_L}{\partial \bar{x}^2}, \quad (8)$$

where $\bar{N} \equiv (\alpha N_T) / (\beta N_L)$ is the non-dimensional density of traps and the non-dimensional lattice diffusion coefficient is $\bar{D}_L \equiv D_L / D_0$. Likewise, the non-dimensional equation for trap kinetics is written in terms of the non-dimensional temperature $\bar{T} \equiv T / T_0$ and vibrational frequency $\bar{\nu} \equiv \nu L^2 / D_0$ as

$$\frac{\partial \theta_T}{\partial \bar{t}} = \frac{\bar{\nu}}{1 + \bar{N}} \left[\exp\left(\frac{-\bar{E}_t}{\bar{T}}\right) \theta_L (1 - \theta_T) - \exp\left(\frac{\bar{\Delta H} - \bar{E}_t}{\bar{T}}\right) \theta_T (1 - \theta_L) \right], \quad (9)$$

where $\bar{\Delta H} \equiv \Delta H / RT_0$ and $\bar{E}_t \equiv E_t / RT_0$.

In the limit $\bar{\nu} \rightarrow \infty$, Eqs. (8) and (9) combine to form a single governing partial differential equation given by

$$\frac{\partial \theta_L}{\partial \bar{t}} \left[1 + \frac{\bar{N} K}{(1 + K \theta_L)^2} \right] + \frac{\bar{N} K \bar{\Delta H} \theta_L \bar{\phi}}{\bar{T}^2 (1 + K \theta_L)^2} = \bar{D}_L \frac{\partial^2 \theta_L}{\partial \bar{x}^2}, \quad (10)$$

where we made use of Eq. (7) to relate θ_T and θ_L and have introduced the non-dimensional heating rate given by $\bar{\phi} \equiv \phi L^2 / T_0 D_0$.

2.3 Analysis of the EP and TDS experiments

Both the EP and TDS experiments can be analysed by solving the governing Eqs. (8) and (9) for finite kinetics of trapping and detrapping, and Eq. (10) for infinitely fast trap/detrap kinetics. The appropriate initial and boundary conditions for both types of experiments are now specified.

Consider first the one-dimensional EP experiment with hydrogen introduced into an initially hydrogen-free specimen of length L at time $t=0$ at the left-hand end of the specimen, $x=0$. With the lattice hydrogen occupancy maintained at θ_L^0 at $x=0$ throughout the test we anticipate that the lattice hydrogen concentration will evolve both temporally and spatially within the specimen as sketched in Fig. 2a. The initial conditions are thus $\theta_L = \theta_T = 0$ for all x and the boundary conditions for $t \geq 0^+$ are specified as $\theta_L(x=0) = \theta_L^0$ and $\theta_L(x=L) = 0$. The flux of hydrogen J measured on the right-hand end (at $x=L$) is given as

$$J(t) = \left(\frac{-D_L \beta N_L}{L} \right) \frac{\partial \theta_L}{\partial \bar{x}} \Big|_{\bar{x}=1}. \quad (11)$$

This flux J represents the number of hydrogen atoms exiting the specimen per unit area per unit time. In the following we shall present a normalised flux $\bar{J} = J / J_{ss}$ where J_{ss} is the steady-state flux given by

$$J_{ss} = \frac{D_L \theta_L^0 \beta N_L}{L}. \quad (12)$$

Now consider the TDS test, again for a one-dimensional specimen of length L . The specimen at time $t=0$ is at temperature T_0 and in equilibrium with a spatially uniform lattice hydrogen occupancy $\theta_L = \theta_L^0$ and the corresponding θ_T given by Eq. (7). At time $t=0^+$, the specimen is begun to be heated at a constant rate ϕ which is sufficiently slow for the temperature to remain spatially uniform such that the temperature varies as a function of time only, and is given by $T = T_0 + \phi t$. Further, we assume that the specimen is heated in a hydrogen-free environment such that for $t > 0^+$, $\theta_L(\bar{x}=0,1) = 0$. The occupancy of lattice hydrogen sites is expected to spatially and temporally evolve as sketched in Fig. 2b. The mass flow rate of atomic hydrogen out of the specimen of cross-sectional area S measured is given as

$$\dot{m}_H = \frac{2JS M_H}{N_A}, \quad (13)$$

where M_H is the molar mass of atomic hydrogen, N_A is Avogadro's constant and J the flux given by Eq. (11). Write m_{FE} as the mass of the specimen. Then, the hydrogen desorption rate per unit mass of the specimen follows as

$$\frac{\dot{m}_H}{m_{FE}} = \frac{2JM_H}{N_A \rho L}, \quad (14)$$

where ρ is the density of the specimen.

3. Analysis of electro-permeation tests

We proceed to predict the isothermal electro-permeation of hydrogen through the specimen in the one-dimensional setting as laid out by the equations of Section 2. First, results are presented to illustrate the role of trap kinetics and then, in the remainder of the section, we restrict attention to the case of local equilibrium (i.e. the Oriani assumption) wherein trap kinetics are assumed to be much faster than the diffusion rate of hydrogen.

3.1 Effect of trap kinetics on permeation tests

The governing equations where the trapping/detrapping rates are finite are given by Eqs. (8) and (9) and we shall restrict attention here to a set of parameters $\bar{N} = 10^{-3}$, $\bar{\Delta H} = -15$, $\bar{E}_t = 0$, $\bar{Q} = 2.75$, $\bar{T} = 1$ and $\theta_L^0 = 10^{-6}$ that is considered to be representative for EP tests in Fe alloys. Predictions of the temporal variation of the normalised flux \bar{J} at $\bar{x}=1$ are included in Fig. 3 for normalised vibrational frequencies in the range

$\bar{\nu} = 10^3 - 10^{12}$. In addition we include the case when $\bar{\nu} \rightarrow \infty$ which corresponds to instantaneous equilibrium between trapped and lattice hydrogen, i.e. the local equilibrium limit with the governing Eq. (10). It is clear that for the realistic range of vibrational frequencies in the range $\bar{\nu} = 10^9 - 10^{12}$ ($\nu = 10^{13} \text{ s}^{-1}$ corresponds to $\bar{\nu} = 10^{14}$ for $D_0 = 10^{-7} \text{ m}^2\text{s}^{-1}$ and $L = 1 \text{ mm}$), the local equilibrium limit provides an excellent approximation to the solution with deviations from this limit only observed at the unrealistic values of $\bar{\nu} \leq 10^3$. Thus, in the remainder of this study we shall assume local equilibrium, and make use of Eq. (10).

3.2. Asymptotic analysis of the local equilibrium limit

Before proceeding to present numerical solutions for the effect of material and loading parameters on the permeation of hydrogen through the specimen in the local equilibrium limit, we develop asymptotic solutions for the governing equation (10). These solutions will highlight the different regimes of behaviour and thereby help in the interpretation of the numerical solutions.

For the purposes of the asymptotic analysis it is instructive to re-write Eq. (10) for the permeation test as

$$\frac{\partial \bar{\theta}_L}{\partial \bar{t}} \left[1 + \frac{\bar{N} K}{(1 + K \theta_L^0 \bar{\theta}_L)^2} \right] = \bar{D}_L \frac{\partial^2 \bar{\theta}_L}{\partial \bar{x}^2}, \quad (15)$$

where $\bar{\theta}_L = \theta_L / \theta_L^0$ such that $0 \leq \bar{\theta}_L \leq 1$. We shall now consider the various limits of this governing partial differential equation (PDE).

Regime I: The low trap occupancy limit with $K \theta_L^0 \ll 1$. Equation (15) then reduces to

$$\frac{\partial \bar{\theta}_L}{\partial \bar{t}} = \left(\frac{\bar{D}_L}{1 + K \bar{N}} \right) \frac{\partial^2 \bar{\theta}_L}{\partial \bar{x}^2}, \quad (16)$$

which is a Fickian diffusion equation with an effective diffusion coefficient

$$\bar{D}_{\text{eff}} = \left(\frac{\bar{D}_L}{1 + K \bar{N}} \right). \quad (17)$$

It has the solution

$$\bar{\theta}_L = \left[1 - \text{erf} \left(\frac{\bar{x}}{2\sqrt{\bar{D}_{\text{eff}} \bar{t}}} \right) \right], \quad (18)$$

in the limit $\sqrt{\bar{D}_{\text{eff}} \bar{t}} \ll 1$. The diffusion distance then scales as $\sqrt{\bar{D}_{\text{eff}} \bar{t}}$ and following [14] we can define the time \bar{t}_{lag} for the hydrogen to reach $\bar{x} = 1$ as $1/(6\bar{D}_{\text{eff}})$, i.e.

$$\bar{D}_L \bar{t}_{\text{lag}} = \frac{1 + K\bar{N}}{6}. \quad (19)$$

Regime II: The deep trap limit with $K\theta_L^0 \gg 1$ and high trap density such that $\frac{\bar{N}}{K(\theta_L^0)^2} \gg 1$.

In this deep trap limit the local equilibrium Eq. (7) gives $\theta_T = 1$ and $\bar{\theta}_L \geq 0^+$ over the domain $0 \leq \bar{x} \leq \bar{\lambda}$. The challenge is to obtain $\bar{\lambda}$ as a function of time. In this domain Eq. (15) reduces to

$$\frac{\partial \bar{\theta}_L}{\partial \bar{t}} \left[\frac{\bar{N}}{K(\theta_L^0)^2 \bar{\theta}_L^2} \right] = \bar{D}_L \frac{\partial^2 \bar{\theta}_L}{\partial \bar{x}^2}. \quad (20)$$

In contrast, over the domain $\bar{\lambda} < \bar{x} \leq 1$, we have $\theta_T = \bar{\theta}_L = 0$. In this high trap density case, the front $\bar{\lambda}$ that demarcates the region with filled and unfilled traps is expected to move slowly as hydrogen needs to diffuse through the lattice over $0 \leq \bar{x} \leq \bar{\lambda}$ and fill the traps at $\bar{x} = \bar{\lambda}$ in order for the front to propagate. It is thus expected that the lattice hydrogen distribution in $0 \leq \bar{x} \leq \bar{\lambda}$ is well approximated by the quasi steady-state solution

$$\bar{\theta}_L = 1 - \frac{\bar{x}}{\bar{\lambda}}. \quad (21)$$

To check, whether Eq. (21) is a solution to (20), we first need to determine the relation $\bar{\lambda}(\bar{t})$. With $\bar{\theta}_L = 0$ at $\bar{x} = \bar{\lambda}$, hydrogen conservation at the front $\bar{\lambda}$ states $J = \dot{\lambda}(\alpha N_T)$, and in normalised form this is written as

$$\bar{J} \bar{D}_L \theta_L^0 = \dot{\lambda} \bar{N}, \quad (22)$$

where $\dot{\lambda} = \dot{\lambda} L / D_0$. Now the normalised flux is given by

$$\bar{J} = -\frac{\partial \bar{\theta}_L}{\partial \bar{x}} = \frac{1}{\bar{\lambda}}, \quad (23)$$

via Eq. (21), from which it follows that

$$\dot{\lambda} = \frac{\bar{D}_L \theta_L^0}{\bar{\lambda} \bar{N}}. \quad (24)$$

Upon substituting Eq. (21) into (20) and using (24) we see that the right hand side of Eq. (20) vanishes while the left hand side reduces to

$$\left[\frac{\bar{N}}{\bar{D}_L K (\theta_L^0)^2 \bar{\theta}_L^2} \right] \frac{\partial \bar{\theta}_L}{\partial \bar{t}} = \frac{1}{K \theta_L^0} \left(\frac{\bar{x}}{\bar{\lambda}^3} \right) \left[1 - \frac{\bar{x}}{\bar{\lambda}} \right]^{-2}. \quad (25)$$

In the limit $K \theta_L^0 \gg 1$ this term tends to zero except at the front $\bar{x} = \bar{\lambda}$, i.e. Eq. (21) is a reasonable approximation of the solution of Eq. (20). The position $\bar{\lambda}$ of the front follows from the solution to (24) with initial conditions $\bar{\lambda}(\bar{t} = 0) = 0$ as

$$\bar{\lambda}^2 = 2 \bar{D}_L \bar{t} \left(\frac{\theta_L^0}{\bar{N}} \right), \quad (26)$$

and the time \bar{t}_{lag} for the front to reach $\bar{\lambda} = 1$ is

$$\bar{D}_L \bar{t}_{\text{lag}} = \frac{1}{2} \left(\frac{\bar{N}}{\theta_L^0} \right). \quad (27)$$

Regime III: The deep trap limit with $K \theta_L^0 \gg 1$ but low trap density such that $\frac{\bar{N}}{K (\theta_L^0)^2} \ll 1$.

Again in this deep trap limit the local equilibrium, Eq. (7) gives $\theta_T = 1$ and $\bar{\theta}_L \geq 0^+$ over the domain $0 \leq \bar{x} \leq \bar{\lambda}$. However, since the trap density is low, Eq. (15) reduces to

$$\frac{\partial \bar{\theta}_L}{\partial \bar{t}} = \bar{D}_L \frac{\partial^2 \bar{\theta}_L}{\partial \bar{x}^2}, \quad (28)$$

which is a Fickian diffusion equation with diffusion constant given by the lattice diffusion coefficient of hydrogen. This admits a solution of the form

$$\bar{\theta}_L = 1 - \text{erf} \left(\frac{\bar{x}}{2 \sqrt{\bar{D}_L \bar{t}}} \right), \quad (29)$$

over $0 \leq \bar{x} \leq \bar{\lambda}$ with $\bar{\lambda} \leq 1$. The position $\bar{\lambda}$ of the front of the trapped hydrogen is again given by mass conservation such that at $x = \lambda$

$$J = \dot{\lambda} \left[\alpha N_T + \beta N_L \theta_L^0 \bar{\theta}_L \Big|_{x=\lambda} \right]. \quad (30)$$

Upon calculating J from Eq. (29), the governing equation for $\bar{\lambda}(\bar{t})$ follows as

$$\dot{\bar{\lambda}} = \frac{\bar{D}_L \theta_L^0 \exp\left[-\left(\frac{\bar{\lambda}}{2\sqrt{\bar{D}_L \bar{t}}}\right)^2\right]}{\sqrt{\pi \bar{D}_L \bar{t}} \left[\bar{N} + \theta_L^0 \left\{ 1 - \operatorname{erf}\left(\frac{\bar{\lambda}}{2\sqrt{\bar{D}_L \bar{t}}}\right) \right\} \right]}, \quad (31)$$

with initial conditions $\bar{\lambda}(\bar{t} = 0) = 0$. There exists no analytical solution to this ordinary differential equation but we can get asymptotic solutions as follows. Note that Eq. (31) will only admit solutions with $\bar{\lambda} \leq 2\sqrt{\bar{D}_L \bar{t}}$, i.e. the front of trapped hydrogen cannot be ahead of the distance the hydrogen would travel in the absence of trapping. This implies that we can consider the following two cases:

Case a: Here $\bar{\lambda} \ll 2\sqrt{\bar{D}_L \bar{t}}$ and we shall subsequently show that this corresponds to a dilute lattice hydrogen concentration such that $\theta_L^0 / \bar{N} \ll 1$. When $\bar{\lambda} \ll 2\sqrt{\bar{D}_L \bar{t}}$, Eq. (31) reduces to

$$\dot{\bar{\lambda}} = \left(\frac{\theta_L^0}{\bar{N} + \theta_L^0} \right) \sqrt{\frac{\bar{D}_L}{\pi \bar{t}}}. \quad (32)$$

Then

$$\bar{\lambda} = 2 \left(\frac{\theta_L^0}{\bar{N} + \theta_L^0} \right) \sqrt{\frac{\bar{D}_L \bar{t}}{\pi}}, \quad (33)$$

upon imposing the initial condition $\bar{\lambda}(\bar{t} = 0) = 0$. The condition $\bar{\lambda} \ll 2\sqrt{\bar{D}_L \bar{t}}$ is satisfied in the limit $\theta_L^0 / \bar{N} \ll 1$, i.e. this solution is applicable when the lattice hydrogen concentration is low compared to the trap density. The time \bar{t}_{lag} for the front to reach $\bar{\lambda} = 1$ is then

$$\bar{D}_L \bar{t}_{\text{lag}} = \frac{\pi}{4} \left(\frac{\bar{N}}{\theta_L^0} \right)^2. \quad (34)$$

Case b: In the oversaturated lattice hydrogen limit with $\theta_L^0 / \bar{N} \approx 1$, Eq. (31) admits the solution $\bar{\lambda} \approx 2\sqrt{\bar{D}_L \bar{t}}$. Thus, the motion of the trapped front is unaffected by the trap density and it immediately follows that the time \bar{t}_{lag} for the front to reach $\bar{\lambda} = 1$ is

$$\bar{D}_L \bar{t}_{\text{lag}} = \frac{1}{6}. \quad (35)$$

Here we have introduced a factor of $1/6$ rather than $1/4$ so that Eq. (19) reduces to Eq. (35) in the limit when $K\bar{N} \rightarrow 0$. We note that, in the absence of traps with $\bar{N} \rightarrow 0$, both regime I and case (b) of regime III reduce to pure lattice diffusion of hydrogen with a diffusion coefficient D_L .

3.2.1 Electro-permeation map

The operative regime is the one associated with the lowest value of $\bar{D}_L \bar{h}_{\text{lag}}$ and then the domains of dominance of the four regimes can be illustrated on a map with axes of $\bar{D}_L \bar{h}_{\text{lag}}$ and θ_L^0 as shown in Fig. 4. At very low θ_L^0 the trap occupancy is negligible with $\bar{D}_L \bar{h}_{\text{lag}}$ independent of θ_L^0 . With increasing θ_L^0 the behaviour transitions to regime II wherein $\bar{D}_L \bar{h}_{\text{lag}}$ is inversely proportional to θ_L^0 . A further increase in θ_L^0 results in the activation of case (a) of regime III (labelled here as regime IIIa) where $\bar{D}_L \bar{h}_{\text{lag}}$ scales inversely with $(\theta_L^0)^2$. Finally at large values of θ_L^0 (regime IIIb), $\bar{D}_L \bar{h}_{\text{lag}}$ again becomes independent of θ_L^0 : here in contrast with regime I, the lattice is oversaturated and the transport of hydrogen reduces to Fickian diffusion with the lattice diffusion coefficient of hydrogen.

We illustrate predictions of the asymptotic analysis in Fig. 5 for selected combinations of $K\bar{N}$ and \bar{N} values again using axes of $\bar{D}_L \bar{h}_{\text{lag}}$ and θ_L^0 . The bottom horizontal line is regime IIIb and independent of $K\bar{N}$ and \bar{N} while the sloping lines are regime IIIa and II: their slopes are fixed as illustrated in Fig. 4 and their positions on the map only dependent on \bar{N} . The other horizontal lines are regime I with their positions a function of the product $K\bar{N}$ such that when $K\bar{N} = 0$, regime I coincides with regime IIIb. The selective dependence of $\bar{D}_L \bar{h}_{\text{lag}}$ on $K\bar{N}$ and \bar{N} suggests a method, which in principle, could be employed to uniquely determine all the relevant diffusion and trapping parameters from EP measurements of \bar{h}_{lag} . This is illustrated as follows. Experiments at large θ_L^0 in regime IIIb where \bar{h}_{lag} is independent of θ_L^0 will give the lattice diffusion constant \bar{D}_L while experiments at lower values of θ_L^0 in regimes IIIa or II will furnish \bar{N} from measurements of \bar{h}_{lag} once \bar{D}_L is known. Finally, measurements of \bar{h}_{lag} at very low values of θ_L^0 in regime I will enable the trapping enthalpy (i.e. K) to be determined given that \bar{D}_L and \bar{N} are already known.

3.3. Numerical predictions and comparisons with the asymptotic analysis

We now proceed to determine the accuracy of the asymptotic analysis presented above. Unless otherwise specified we will consider a representative material with $\overline{\Delta H} = -13.82$ ($K = 10^6$), $\overline{Q} = 2.75$, $\overline{N} = 10^{-3}$ and $\overline{T} = 1$ and present numerical predictions of permeation experiments for selected values of θ_L^0 such that the behaviour spans across the regimes presented above. The governing PDE, Eq. (10) was solved using the *pdepe* partial differential equation solver in MATLAB. The *pdepe* solver has an automatic time-stepping routine to ensure temporal convergence with the spatial discretisation provided as an input. All simulations used a uniform mesh with mesh size $e = 0.005L$: mesh sensitivity studies confirmed that this spatial resolution was sufficient for all the regimes analysed here.

Regime I: With $\theta_L^0 = 10^{-7}$, we expect the response to be within regime I from the map in Fig. 5. Numerical predictions of the temporal variation of \overline{J} at $\overline{x} = 1$ are included in Fig. 6a along with predictions of the spatial distributions of θ_L / θ_L^0 at selected times in Fig. 6b. In regime I, the asymptotic analysis suggests a Fickian diffusion process with an effective diffusion coefficient $\overline{D}_{\text{eff}} \approx \overline{D}_L / (K\overline{N})$. In line with this we see that a finite hydrogen flux is measured at $\overline{x} = 1$ when the normalised time $\overline{D}_L \overline{t}$ is on the order of $K\overline{N}$. Subsequently, as would be expected for a diffusion process the flux rises gradually until a steady-state is achieved. This picture is also confirmed by the distribution of θ_L / θ_L^0 in Fig. 6b which demonstrate that early in the time history θ_L / θ_L^0 has an error function like variation with a linear spatial distribution of θ_L / θ_L^0 achieved at long times when steady-state is attained. The asymptotic predictions (18) of the spatial variation of θ_L / θ_L^0 are included in Fig. 6b and show excellent agreement with the numerical predictions when $\overline{D}_L \overline{t} \ll 1$, i.e. before the diffusion process starts to interact strongly with the $\overline{x} = 1$ boundary.

Regime II: With $\theta_L^0 = 10^{-4}$, we anticipate the response to be within regime II. Here the asymptotic analysis predicts that a linear spatial distribution of θ_L / θ_L^0 is attained behind the front that demarcates the regions where $\theta_T = 1$ and $\theta_T = 0$. Numerical and asymptotic predictions of the spatial distributions of θ_L / θ_L^0 are included in Fig. 6c at selected values of $\overline{D}_L \overline{t}$. Excellent agreement between the two sets of predictions is seen. The corresponding numerical prediction of \overline{J} versus $\overline{D}_L \overline{t}$ in Fig. 6a confirms that there is a sharp increase in \overline{J} at $\overline{x} = 1$ when the front of trapped hydrogen reaches $\overline{x} = 1$. This is in contrast to regime I where the Fickian diffusion nature of the governing equations implies \overline{J} rises more gradually.

Regime IIIb: With $\theta_L^0 = 10^{-2}$, we anticipate the response to be within regime IIIb. Comparisons between the numerical and asymptotic predictions of the spatial distributions of θ_L / θ_L^0 at selected values of $\bar{D}_L \bar{t}$ are included in Fig. 6d. Reasonable agreement is observed for $\bar{D}_L \bar{t} < 1$, although the asymptotic analysis over predicts the concentrations near the front that demarcates the regions where $\theta_T = 1$ and $\theta_T = 0$. Again, consistent with the fact the hydrogen is present only behind this front, the \bar{J} versus $\bar{D}_L \bar{t}$ curve in Fig. 6a shows a sharp increase when this front reaches $\bar{x} = 1$, i.e. at $\bar{D}_L \bar{t} \approx 1/6$. We note in passing that numerical predictions for regime IIIa are not included as this regime spans a very narrow range in θ_L^0 as seen in Fig. 5. Thus, the numerical predictions directly transition from regime II to regime IIIb with regime IIIa not being clearly distinguished.

We proceed to illustrate the accuracy of the asymptotic analysis over a wide range of parameters by including numerical predictions of $\bar{D}_L \bar{t}_{\text{lag}}$ on the map in Fig. 5. In this regard we performed a series of numerical calculations with $\bar{\Delta H} = -13.82$ ($K = 10^6$), $\bar{Q} = 2.75$ and $\bar{T} = 1$ held fixed (i.e. the reference properties employed above) and varying \bar{N} and θ_L^0 over the ranges $10^{-5} \leq \bar{N} \leq 10^{-2}$ and $10^{-7} \leq \theta_L^0 \leq 10^{-2}$. In these numerical calculations, following Barrer [14], we define \bar{t}_{lag} as the normalised time when $\bar{J} = 0.632$, i.e. the time when the flux attains 63.2% of its steady-state value. Numerical predictions of $\bar{D}_L \bar{t}_{\text{lag}}$ are included in Fig. 5 and show excellent agreement with the asymptotic analysis over a very wide range of parameters. As is expected the asymptotic analysis loses accuracy at the boundaries of the regimes. Moreover, at low $K\bar{N}$ the asymptotic analysis is again inaccurate as in this case regimes I and regime IIIb have very similar time lag values and thus the entire response lies intermediate to these regimes. In addition to these numerical calculations we have also included in Fig. 5, predictions of $\bar{D}_L \bar{t}_{\text{lag}}$ as a function of θ_L^0 for $K = 10^5$ and $\bar{N} = 10^{-3}$ with the other properties held fixed at their reference values. These predictions are also in good agreement with the asymptotic analysis and confirm that within regime II, $\bar{D}_L \bar{t}_{\text{lag}}$ is insensitive to K ; see the overlap in Fig. 5 between the predictions with $K = 10^5$ and 10^6 .

The map in Fig. 5 is over a very wide range of parameters with large portions of the map mostly inaccessible for typical hydrogen electro-permeations experiments in Fe alloys. It is thus instructive to examine the response over a range of parameters more representative in such experiments. In this regard we include in Figs. 7a and 7b numerical predictions of contours of $\bar{D}_L \bar{t}_{\text{lag}}$ (with \bar{t}_{lag} defined as above) for $\theta_L^0 = 10^{-6}$ and 10^{-7} , respectively

for a test temperature $\bar{T} = 1$. These contours are presented on a map with axes of \bar{N} and $\overline{\Delta H}$: in line with the predictions in Fig. 5 we observe that $\bar{D}_L \bar{t}_{\text{lag}}$ increases with decreasing $\overline{\Delta H}$ (deeper traps), increasing trap density \bar{N} and decreasing hydrogen concentration θ_L^0 . Moreover, the contours of $\bar{D}_L \bar{t}_{\text{lag}}$ suggest that there is a regime where \bar{t}_{lag} is independent of $\overline{\Delta H}$ and another where \bar{t}_{lag} increases linearly with \bar{N} . In fact, the asymptotic analysis indicates that both the maps in Fig. 7 span regimes I and II with the boundary between the two regimes given by a transition value of the binding energy

$$K_{I-II} \equiv \exp(-\overline{\Delta H}_{I-II}) = \frac{3}{\theta_L^0} - \frac{1}{\bar{N}}. \quad (36)$$

This boundary is indicated in Fig. 7 with \bar{t}_{lag} independent of $\overline{\Delta H}$ in regime II (i.e. deep trap regime). Selected asymptotic predictions of $\bar{D}_L \bar{t}_{\text{lag}}$ are also included in Fig. 7 and confirm that over this more representative parameter range the asymptotic predictions are an excellent approximation of the complete numerical calculations.

4. Application of the model to EP and TDS measurements

The EP analysis presented above illustrates that experiments need to span across regimes I, II and IIIb in order to uniquely determine the three main material parameters, viz. \bar{N} , $\overline{\Delta H}$ and \bar{D}_L . Further, these parameters extracted from an EP measurement would only represent true estimates of the material properties if predictions using these parameters also provided good agreement with TDS measurements for the same material. With this in mind, we proceed in two steps. First, we attempt to determine \bar{N} , $\overline{\Delta H}$ from room temperature EP tests on a quenched and tempered martensitic steel Fe–0.45C–1.5Mo reported by Frappart et al. [15]. These parameters are then used to make predictions of the thermal desorption measurements reported by Frappart et al. [16] on the same steel.

Frappart et al. [15] performed EP tests using the Devanathan and Stachursky [17] EP apparatus on martensitic steel specimens of length $L = 1.1$ mm and cross-section area 3.14 cm^2 at a temperature $T_0 = 293$ K. In these tests, the input charging current was varied in order to perform tests at different hydrogen charging conditions θ_L^0 and the temporal variation of the current output $i(t)$ per unit area was measured. These measurements are included in Fig. 8 in terms of the output flux J of atomic hydrogen with $J \equiv i / (FZ)$, where F represents the Faraday constant and $Z = 1$ being the state of charge of the atomic hydrogen. The steady-state flux J_{ss} is used

to estimate θ_L^0 via Eq. (12) using the room temperature lattice diffusion coefficient of hydrogen in martensitic steel $D_L = 1.65 \times 10^{-9} \text{ m}^2 \text{ s}^{-1}$ [15] and $\beta N_L = 8.46 \times 10^{28} \text{ m}^{-3}$ [7]. The curves in Fig. 8 for the different input currents are labelled by their θ_L^0 values calculated in this manner.

In line with the procedure outline in section 3 we define \bar{t}_{lag} as the time when $J = 0.632 J_{ss}$. The measurements of the normalised time lag $\bar{D}_L \bar{t}_{\text{lag}}$ as a function of θ_L^0 are summarised in the map in Fig. 9 along with the asymptotic predictions with $K\bar{N} = 28$ and selected values of \bar{N} in the range $10^{-5} \leq \bar{N} \leq 10^{-3}$. It is clear from this map that all measurements lie in regime I with $K\bar{N} = 28$ fitting the measurements to within the scatter in the data. The fact that all the data lie in regime I implies that the data is insufficient to uniquely determine both K (or $\overline{\Delta H}$) and \bar{N} except to say that we expect $\bar{N} > 10^{-5}$ with $K\bar{N} = 28$ ($\bar{N} < 10^{-5}$ would imply that the response transitions to regime II at the higher values of θ_L^0 investigated in [15] but this is not supported by the measurements). To emphasize this point we include in Fig. 8a numerical predictions of the temporal variation of flux J at a temperature $\bar{T} = 1$ with $\bar{N} = 1.7 \times 10^{-4}$ and $\overline{\Delta H} = -12$ as well as $\bar{N} = 1.26 \times 10^{-3}$ and $\overline{\Delta H} = -10$ in Fig. 8b such that $K\bar{N} = 28$ in both cases but \bar{N} varies by nearly an order of magnitude between the two cases. Excellent agreement is observed between the measurements and numerical predictions in both cases demonstrating the inadequacy of the data to uniquely determine both the trap density and binding energy from EP measurements that all lie in regime I.

The TDS measurements of Frappart et al. [16] are included in Fig. 10 on specimens of cross-sectional area $S = 40 \text{ mm}^2$ and length $L = 4 \text{ mm}$. The TDS tests were carried out starting from an initial temperature $T_0 = 353 \text{ K}$ and the three heating rates ϕ listed in Fig. 10. Since these specimens were made from the steel on which the EP measurements discussed above were reported, we now proceed to present desorption predictions using the \bar{N} and K values estimated above and the lattice activation energy taken to be $Q = 10 \text{ kJ mol}^{-1}$ [15]. However, the hydrogen loading parameter θ_L^0 in the TDS experiment is unknown and, unlike in the EP tests where it is directly obtained from J_{ss} , cannot be directly inferred from the TDS measurements. We thus use θ_L^0 as a fitting parameter in order to get good agreement between predictions and measurements of the peak desorption rates. The desorption predictions with $\bar{N} = 1.7 \times 10^{-4}$ and $\overline{\Delta H} = -12$ (i.e. the values used for the EP predictions of Fig. 8a) using $\theta_L^0 = 4.2 \times 10^{-3}$ are included in Fig. 10. Unlike in the measurements, the model does not predict a distinct peak at an intermediate temperature and thus we chose θ_L^0 such that the peak desorption

rate measurements matched the desorption rate at which there is an inflexion in the predicted desorption curves. Beyond the inflexion, the measurements and predictions are in excellent agreement and we argue that measurements do not accurately capture the initial transient because hydrogen has started to leak out of the specimen prior to the commencement of the measurements as discussed in Raina et al. [13]. For the sake of brevity we do not include predictions with $\bar{N} = 1.26 \times 10^{-3}$ and $\overline{\Delta H} = -10$ (i.e. the values used for the EP predictions of Fig. 8b) but it suffices to say that similar agreement with the measurements is obtained in this case as well with the choice $\theta_L^0 = 3 \times 10^{-3}$.

Two key conclusions can be drawn from this attempt at comparing simulations and measurements: (i) EP measurements that do not span regimes cannot uniquely provide the material parameters related to the traps and (ii) trapping parameters estimated from EP tests can be used to obtain a good agreement between predictions and measurements from TDS tests. The hydrogen charging in TDS tests, which is parameterised by θ_L^0 , needs to be used as a fitting parameter in this case.

5. Concluding remarks

The McNabb and Foster [1] framework is used to analyse both electro-permeation (EP) and thermal desorption (TDS) measurements of hydrogen in metallic alloys. The framework includes the diffusion of hydrogen through the lattice as well as the trapping (and detrapping) of hydrogen at specific sites that might include dislocations, carbide particles and grain boundaries. It is shown that the trapping and detrapping rates are typically much faster compared to the diffusion time-scales and a simplification of the governing equations wherein we assume local equilibrium between the lattice and trapped hydrogen suffices.

An asymptotic analysis of the governing kinetic equation for the EP test is presented. This asymptotic analysis reveals that there are four regimes of behaviour. In regime I the trapping is negligible and hydrogen kinetics is governed by a Fickian diffusion equation with an effective diffusion coefficient that can be significantly smaller than the lattice hydrogen diffusion coefficient. Regimes II and III are high trap occupancy regimes with regime II corresponding to a high trap density while the trap density is low in regime III. In both these regimes there exists a demarcation front that divides the specimen into regions with filled and unfilled traps. Regime III comprises of two sub-regimes with the regime labelled regime IIIb corresponding to the case of oversaturated lattice hydrogen. In this regime hydrogen transport occurs at a rate governed solely by the lattice hydrogen diffusion coefficient. The asymptotic analysis clearly reveals that EP tests need to span regimes I, II and IIIb in order to uniquely extract all the relevant material properties related to hydrogen transport. Numerical solution of the governing diffusion equation confirmed the accuracy of the asymptotic analysis.

Numerical simulations of EP and TDS tests on the same material, as reported by Frappart et al. [15, 16], are presented. The EP measurements are shown to all lie in regime I and are thus insufficient to uniquely determine both the trap density and binding energy. However, with trapping parameters estimated from the EP tests, the model is shown to capture the TDS tests with reasonable accuracy. Future studies wherein EP and TDS measurements are carried out on the same material with the EP tests spanning across the different regimes of behaviour are suggested in order to further confirm the fidelity of the model in predicting hydrogen kinetics in metallic alloys.

Additional Information

Ethics

The research work did not involve active collection of human data or any other ethical issues.

Data Accessibility

All presented numerical results can be reproduced with the in-built `pdepe` solver of Matlab® Software

Authors' Contributions

All authors contributed equally to this work. All authors gave final approval for publication.

Competing Interests

The authors declare that they have no competing interests.

Funding Statement

The authors would like to acknowledge the funding and technical support from BP through the BP International Centre for Advanced Materials (BP-ICAM) which made this research possible.

References

1. McNabb A, Foster PK. 1963 A new analysis of the diffusion of hydrogen in iron and ferritic steels. *Trans. Metall. Soc. AIME.* **227**, 618-627.
2. Bhadeshia HKDH. 2016 Prevention of Hydrogen Embrittlement in Steels. *ISIJ Int.* **56(1)**, 24-36.
3. Song EJ, Suh D-W, Bhadeshia HKDH. 2013 Theory for hydrogen desorption in ferritic steel. *Comp. Mat. Sci.* **79**, 36-44.
4. Ebihara K, Kaburaki H, Suzudo T and Takai K. 2009 A Numerical Study on the Validity of the Local Equilibrium Hypothesis in Modeling Hydrogen Thermal Desorption Spectra. *ISIJ Int.* **49(12)**, 1907-1913.

-
5. Kissinger HE. 1956 Variation of peak temperature with heating rate in differential thermal analysis. *J. Research Nat. Bur. Std.* **57(4)**, 217-221.
 6. Oriani RA. 1970 The diffusion and trapping of hydrogen in steel. *Acta Metall.* **18**, 147-157.
 7. Sofronis P, McMeeking RM. 1989 Numerical analysis of hydrogen transport near a blunting crack tip. *J. Mech. Phys. Solids* **37(3)**, 317-350.
 8. Thomas RLP, Li Daoming, Gangloff RP and Scully JR. 2002 Trap-Governed Hydrogen Diffusivity and Uptake Capacity in Ultrahigh-Strength AERMET 100 Steel. *Metall. Mat. Trans. A* **33A**, 1991-2004.
 9. Turnbull A, Carroll MW, Ferriss DH. 1989 Analysis of hydrogen diffusion and trapping in a 13% Chromium martensitic steel. *Acta Metall.* **37(7)**, 2039-2046.
 10. Turnbull A, Hutchings RB, Ferriss DH. 1997 Modelling of thermal desorption of hydrogen from metals. *Mat. Sci. Engrg.* **A238**, 317-328.
 11. Turnbull A. 2015 Perspectives on hydrogen uptake, diffusion and trapping. *Int. J. Hydrogen Energy*, **40**, 16961-16970.
 12. Ha HM, Ai J-H and Scully JR. 2014 Effects of Prior Cold Work on Hydrogen Trapping and Diffusion in API X-70 Line Pipe Steel During Electrochemical Charging. *Corrosion.* **70(2)**, 166-184.
 13. Raina A, Deshpande VS, Fleck NA. 2016 Method for the determination of trap characteristics from the thermal desorption of hydrogen in metals. *submitted for publication in Acta Mater.*
 14. Barrer RM. 1941 Diffusion in and through solids. *Cambridge University Press.*
 15. Frappart S, Feaugas X, Creus J, Bouhattate J, Thébault F, Delattre L, Marchebois H. 2010 Study of the hydrogen diffusion and segregation into Fe-C-Mo martensitic HSLA steel using electrochemical permeation test. *J. Phys. Chem. Solids.* **71**, 1467-1479.
 16. Frappart S, Oudriss A, Feaugas X, Creus J, Bouhattate J, Thébault F, Delattre L, Marchebois H. 2011 Hydrogen trapping in martensitic steel investigated using electrochemical permeation and thermal desorption spectroscopy. *Scr. Mater.* **65**, 859-862.
 17. Devananthan MAV and Stachurski Z. 1964 The Mechanism of Hydrogen Evolution on Iron in Acid Solutions by Determination of Permeation Rates. *J. Electrochemical Soc.* **111(5)**, 619-623.

Figures

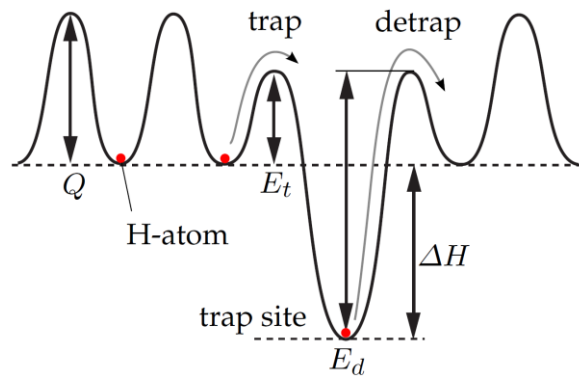


Figure 1: Sketch of the energy landscape for the kinetics of hydrogen through a lattice with trapping sites. The energy barrier for diffusion through the lattice is Q while E_t and $E_d = E_t - \Delta H$ are the trapping and detrapping energy barriers, respectively.

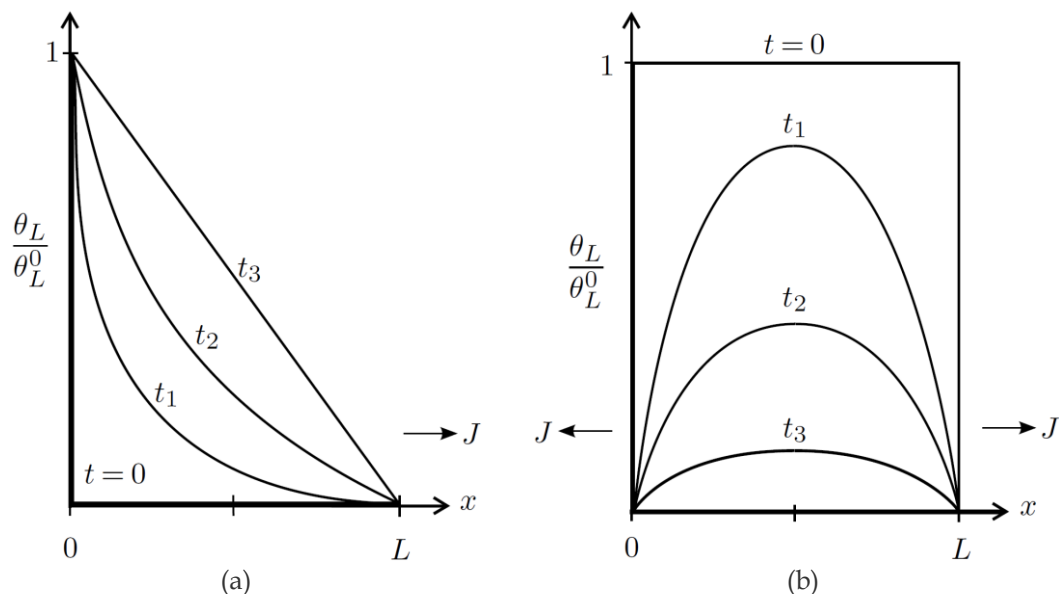


Figure 2: Sketch of the spatio-temporal evolution of the normalised lattice hydrogen occupancy θ_L / θ_L^0 in the (a) electro-permeation (EP) and (b) thermal desorption (TDS) tests. In both cases, the one-dimensional specimen spans $0 \leq x \leq L$ and curves are shown at selected times $0 < t_1 < t_2 < t_3$. The output flux J is also indicated in both cases.

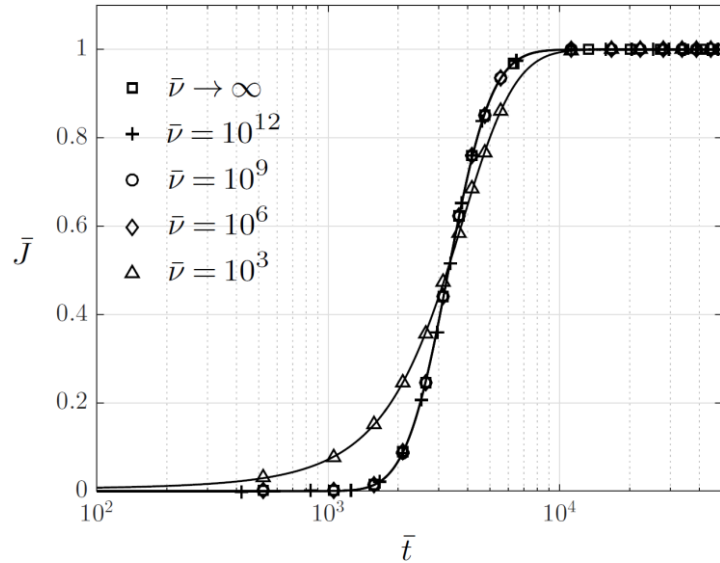


Figure 3: Predictions of the temporal evolution of the normalised output flux \bar{J} in an EP test with material parameters $\bar{N}=10^{-3}$, $\bar{\Delta H}=-15$, $\bar{E}_t=0$, $\bar{Q}=2.75$, $\bar{T}=1$ and hydrogen loading $\theta_L^0=10^{-6}$. Results are shown for normalised vibrational frequencies in the range $\bar{\nu}=10^3-10^{12}$ as well as the local equilibrium limit with $\bar{\nu} \rightarrow \infty$.

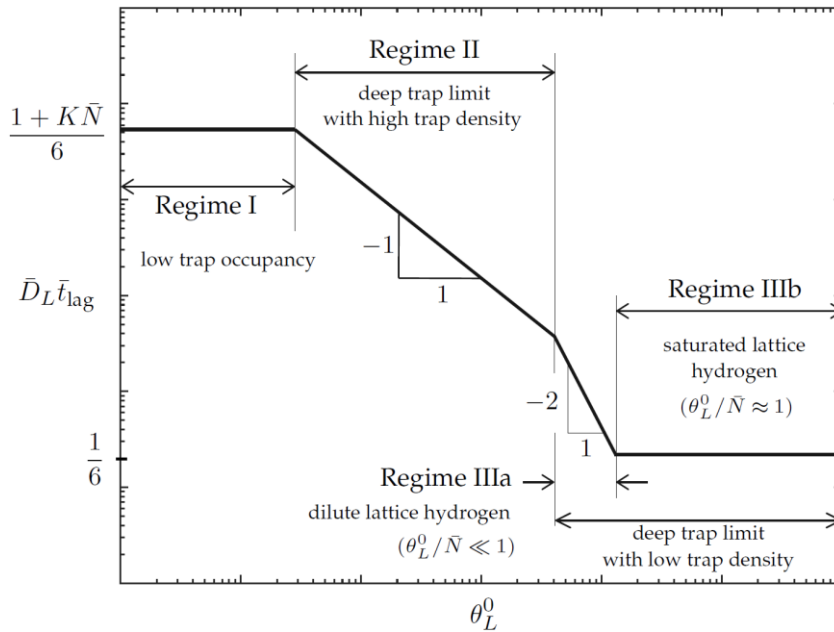


Figure 4: Sketch illustrating the four regimes of behaviour as deduced from the asymptotic analysis of the EP test. The regimes are marked on the map with axes of normalised time lag $\bar{D}_L \bar{t}_{\text{lag}}$ and input lattice hydrogen occupancy θ_L^0 . The value of $\bar{D}_L \bar{t}_{\text{lag}}$ in regimes I and IIIb is indicated, with $\bar{D}_L \bar{t}_{\text{lag}}$ in regimes II and IIIa only dependent on θ_L^0 and \bar{N} .

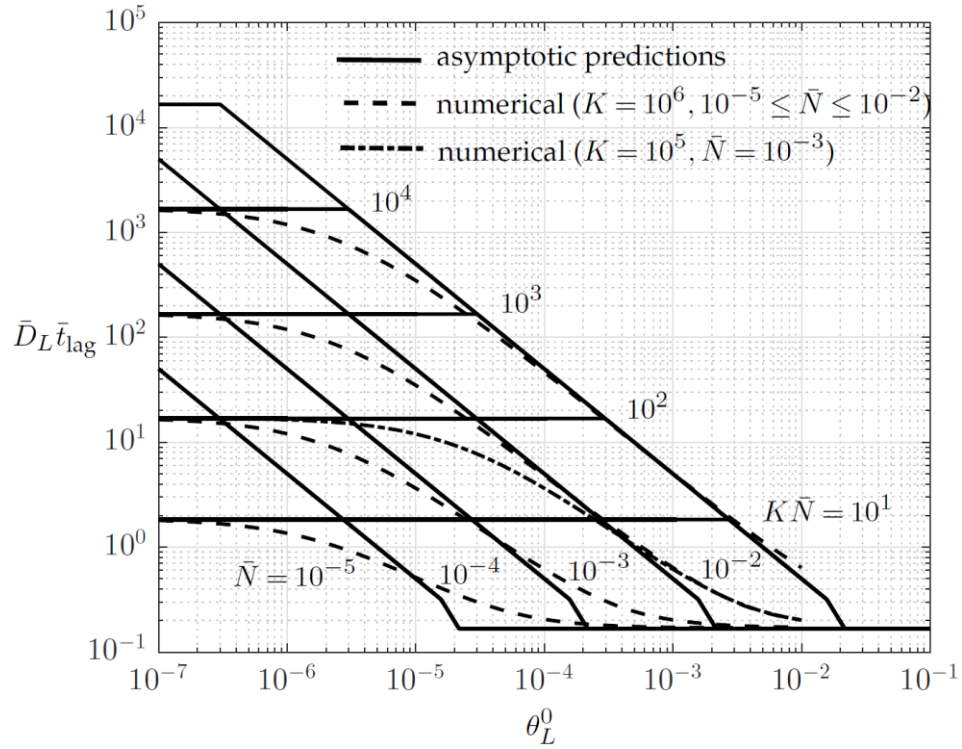


Figure 5: A map summarising the dependency of the normalised time lag $\bar{D}_L \bar{t}_{\text{lag}}$ in the EP test on the trapping parameters K and \bar{N} as well as the hydrogen loading parameterised by θ_L^0 . The map includes both asymptotic predictions and numerical predictions for selected values of K and \bar{N} .

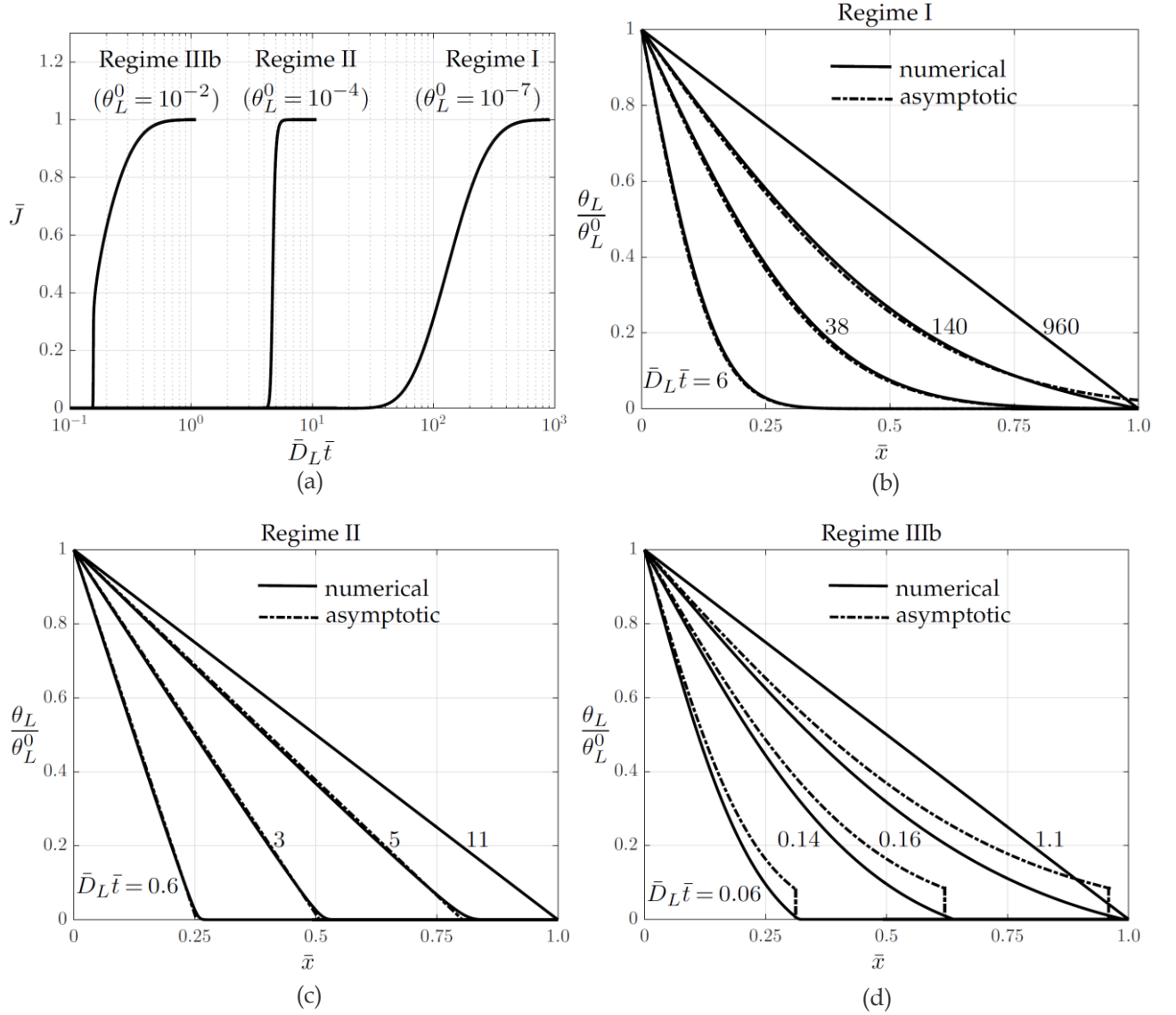


Figure 6: Comparisons of the asymptotic and numerical predictions of the transient response in EP tests in three regimes for a reference set of material parameters $\overline{\Delta H} = -13.82$ ($K = 10^6$), $\bar{Q} = 2.75$, $\bar{N} = 10^{-3}$ and $\bar{T} = 1$. (a) Numerical predictions of the temporal evolution of the normalised output flux \bar{J} in regime I ($\theta_L^0 = 10^{-7}$), regime II ($\theta_L^0 = 10^{-4}$) and regime IIIb ($\theta_L^0 = 10^{-2}$). The corresponding numerical and asymptotic predictions of the spatio-temporal evolution of the normalised lattice hydrogen occupancy θ_L / θ_L^0 in (b) regime I, (c) regime II and (d) regime IIIb.

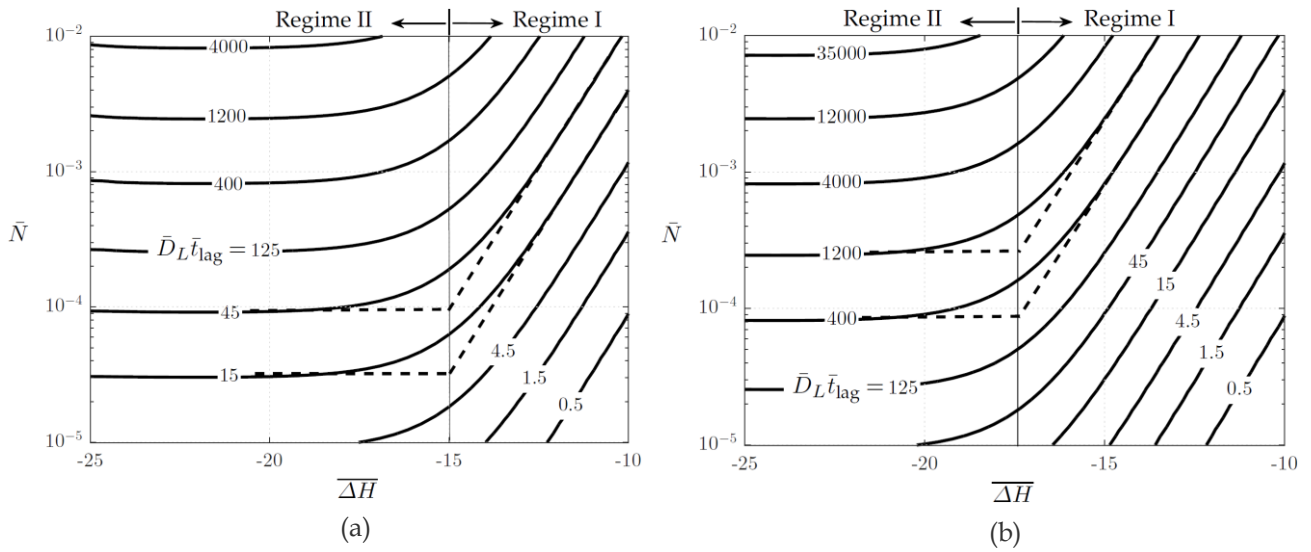


Figure 7: Maps showing contours of the normalised time lag $\bar{D}_L \bar{t}_{lag}$ in an EP test using axes of the normalised trap density \bar{N} and the normalised trap binding energy $\bar{\Delta H}$ (with $\bar{T}=1$) for hydrogen loading with (a) $\theta_L^0 = 10^{-6}$ and (b) $\theta_L^0 = 10^{-7}$. Both maps only span regimes I and II with the solid lines corresponding to numerical predictions and selected asymptotic predictions indicated by dashed lines.

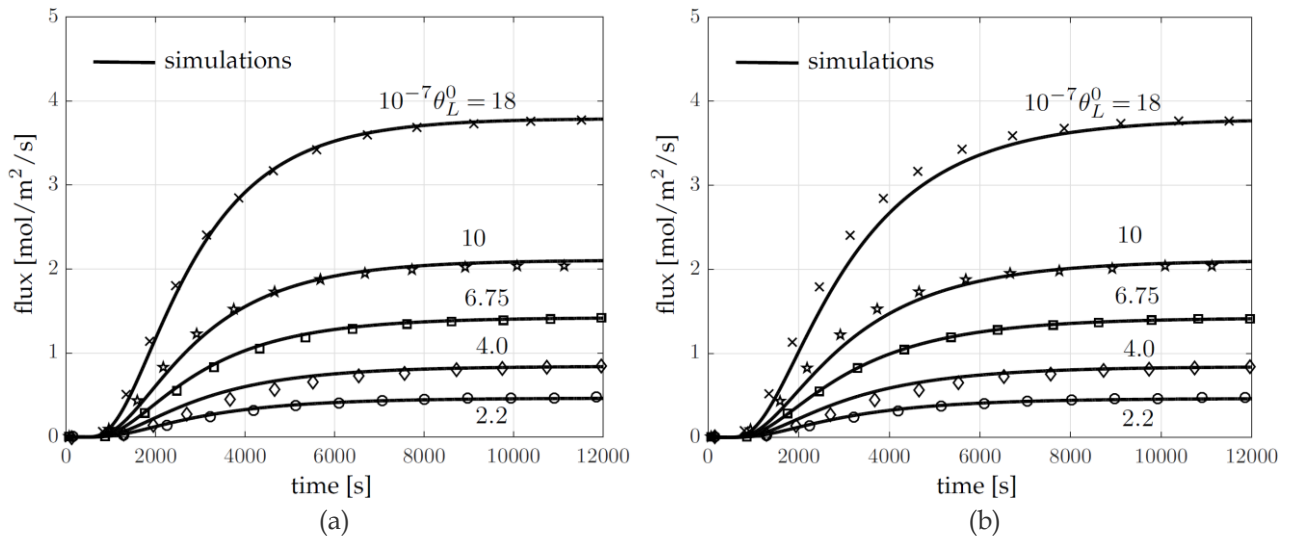


Figure 8: Comparisons between numerical predictions and measurements [15] of the temporal evolution of the output flux in EP tests on a quenched and tempered martensitic steel Fe–0.45C–1.5Mo. The measurements are shown (by markers) for selected input currents parameterised here by θ_L^0 along with numerical predictions employing (a) $\bar{N} = 1.7 \times 10^{-4}$ and $\bar{\Delta H} = -12$ and (b) $\bar{N} = 1.26 \times 10^{-3}$ and $\bar{\Delta H} = -10$ for a test temperature $\bar{T} = 1$.

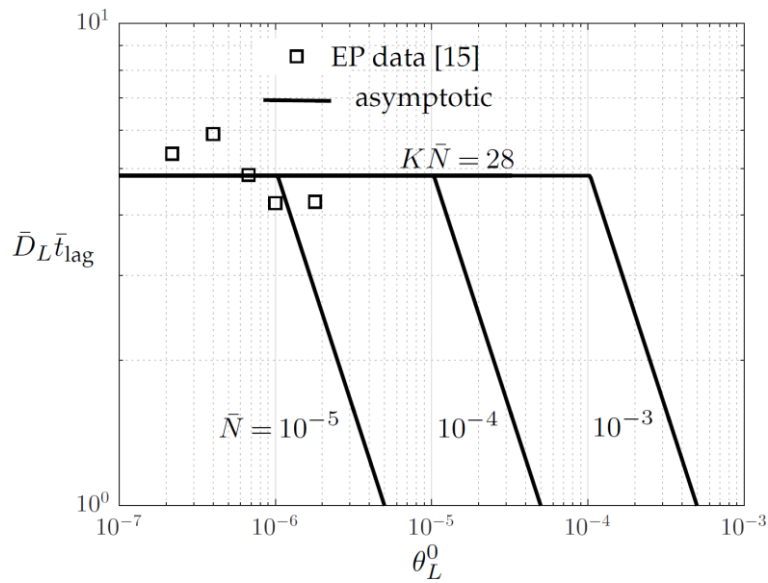


Figure 9: A summary of the time lag measurements from the data in Fig. 8 on a map using axes of $\bar{D}_L \bar{t}_{lag}$ and the input lattice hydrogen occupancy θ_L^0 . Asymptotic predictions in regimes I and II are indicated for $K\bar{N} = 28$ and selected values of \bar{N} .

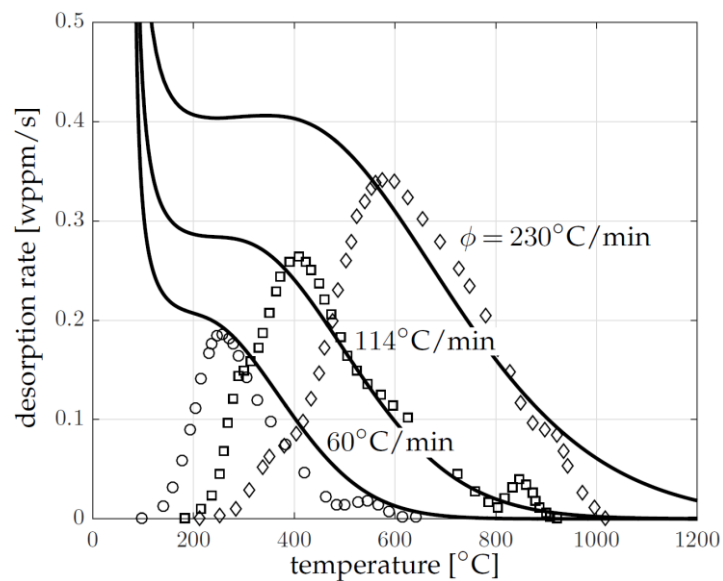


Figure 10: Comparison between measured (shown by markers) and predicted (solid lines) desorption curves for TDS tests [16] carried out on a quenched and tempered martensitic steel Fe–0.45C–1.5Mo. Both measurements and predictions are shown for three heating rates ϕ , an initial lattice hydrogen occupancy $\theta_L^0 = 4.2 \times 10^{-3}$ and trap properties used in Fig. 8a.